Countergradient momentum flux in the presence of rolls in the atmospheric boundary layer

Additional thesis in Geoscience & Remote Sensing

Ho Yi Lydia Mak

Delft University of Technology

TU Delft

Countergradient momentum flux in the presence of rolls in the atmospheric boundary layer

by

Ho Yi Lydia Mak

Student number:	5540453	
Project duration:	December, 2022 - February, 2023	
Thesis committee:	Stephan de Roode	TU Delft, Supervisor
	Fredrik Jansson	TU Delft
	Louise Nuijens	TU Delft

Abstract

In the atmospheric boundary layer, when surface heat flux is small and mean wind shear is strong, horizontal convective rolls that are elongated along the wind shear are formed. This study attempts to explain the asymmetry of rolls in terms of turbulence using large-eddy simulations. A pressure gradient in the north-south y direction is applied, which results in an east-west geostrophic wind U_g. It is shown that the turbulent kinetic energy components in the x and y directions are not equal when rolls develop. In addition, a countergradient regime is present for vertical momentum flux in the y direction ($\overline{v'w'}$) in convective boundary layer with rolls. In the countergradient regime, the wind variance in the y direction ($\overline{v'^2}$) is destroyed, contrary to being produced in the x direction. The presence of a countergradient regime for $\overline{v'w'}$ but not $\overline{u'w'}$ suggests that the eddy viscosity in the x and y directions would be rather different, and even become negative for $\overline{v'w'}$. Thus, the existing parameterization scheme in global atmospheric models may need to be modified. However, the design of an improved parameterization scheme is non-trivial as the countergradient regime is non-stationary when stability decreases, while it does not exist in neutral or stable boundary layers with rolls.

Contents

1
Introduction

In the atmospheric boundary layer, the structure of large-scale shallow convection is controlled by buoyancy and mean wind shear. When surface buoyancy flux is large and mean wind shear is weak, open convective cells which consists of ascending motion with clouds in the walls and descending motion in the cloud free center are formed; when the surface heat flux is small and mean wind shear is strong, horizontal convective rolls that are aligned within 10–20° of the mean wind direction are formed [1].

In the study of Salesky et al. (2017) who used large-eddy simulations (LES) to study the transition from rolls to cells, it was found that the transition occurs gradually as $-z_i/L$ increases from 0 (neutral condition) to ∞ (free convective condition). Here, z_i is the convective boundary layer depth and

$$L = \frac{-u_*^3\theta_0}{\kappa g Q_0} \tag{1.1}$$

is the Obukhov length, where u_* is the friction velocity, θ_0 is the mean surface temperature, κ is the von Kármán constant, g is the gravitational acceleration, and Q_0 is the kinematic surface heat flux. They have performed in depth analysis of the mean vertical profiles of velocity variances, turbulent transport efficiencies, as well the “roll factor”, which characterizes the rotational symmetry of the vertical velocity field, to identify the transition from rolls to cells. However, they have not looked into the turbulent kinetic energy (TKE) budget when rolls develop, as well as how the parameterization of fluxes in the atmosphere might be different when rolls and cells develop respectively.

This study aims to understand how roll structures are formed by looking at the turbulence in the boundary layer. Since rolls are asymmetric in the x and y directions, it would be interesting to investigate the asymmetry of $\overline{u'^2}$ and $\overline{v'^2}$ and the shear generation term in the x and y directions in the TKE budget. This will be done using Dutch Atmospheric Large-Eddy Simulation (DALES) following the simulation cases set up by Salesky et al. Moreover, in weather forecast models, eddy viscosity profiles in the x and y directions are usually assumed to be the same, yet the asymmetrical structure of rolls in the x and y directions suggests that they may be asymmetrical. Therefore, the eddy viscosity profiles will also be diagnosed to give insights into how the parameterization of momentum fluxes could be improved in weather and climate models.

2
Theory

2.1. DALES

Large-eddy simulation (LES) is an approach to model the atmosphere through resolving turbulent scales larger than a chosen filter width, while parameterizing the smaller ones. In the Dutch Atmospheric Large-Eddy Simulation (DALES), the governing equations are [2]

$$\frac{\partial \widetilde{u_i}}{\partial x_i} = 0, \tag{2.1}$$

$$\frac{\partial \widetilde{u_i}}{\partial t} = -\frac{\partial \widetilde{u_i}\widetilde{u_j}}{\partial x_j} - \frac{\partial \pi}{\partial x_i} + \frac{g}{\theta_0}\widetilde{\theta_v}\delta_{i3} + \mathcal{F}_i - \frac{\partial \tau_{ij}}{\partial x_j}, \tag{2.2}$$

$$\frac{\partial \widetilde{\varphi}}{\partial t} = -\frac{\partial \widetilde{u_j}\widetilde{\varphi}}{\partial x_j} - \frac{\partial R_{u_j,\varphi}}{\partial x_j} + \mathcal{S}_{\varphi}, \tag{2.3}$$

which represent the conservation of mass, momentum and energy respectively. The tildes denote the filtered mean variables. π is the modified pressure, δ_{ij} is the Kronecker delta, $\mathcal{F}_i$ represents other forcings, such as large scale forcings and Coriolis acceleration, τ_{ij} is the sub-grid momentum flux and $\mathcal{S}_{\varphi}$ denotes source terms for scalar φ. $R_{u_j,\varphi} \equiv \widetilde{u_j\varphi} - \widetilde{u_j}\widetilde{\varphi}$ is the subfilter-scale (SFS) flux.

2.2. Turbulent Kinetic Energy

In this study, we are interested in the turbulent kinetic energy (TKE) in the boundary layer, which is defined as

$$e = \frac{1}{2}(\overline{u'^2} + \overline{v'^2} + \overline{w'^2}), \tag{2.4}$$

where overbars and primes denote the slab mean and fluctuation of the variables respectively.

From the prognostic equations of $\widetilde{u_i}$, one can apply Reynolds decomposition (Equation 2.5) followed by Reynolds averaging. For simplicity, the tildes will be omitted from now on.

$$u_i = \overline{u_i} + u_i' \tag{2.5}$$

After subtracting the mean state, the prognostic equations of u_i' are obtained. Multiplying them by u_i' and averaging, the prognostic equations of $u_i'^2$ are obtained, which are the budget equations of the three components of TKE. When mean horizontal advection is assumed to be zero, the budget equations are given as [3]:

$$\frac{1}{2}\frac{\partial \overline{u'^2}}{\partial t} = -\overline{u'w'}\frac{\partial \overline{u}}{\partial z} - \frac{1}{\overline{\rho}}\overline{u'\frac{\partial p'}{\partial x}} - \frac{1}{2}\frac{\partial \overline{w'u'u'}}{\partial z} - \epsilon_u, \tag{2.6}$$

$$\frac{1}{2}\frac{\partial \overline{v'^2}}{\partial t} = -\overline{v'w'}\frac{\partial \overline{v}}{\partial z} - \frac{1}{\overline{\rho}}\overline{v'\frac{\partial p'}{\partial y}} - \frac{1}{2}\frac{\partial \overline{w'v'v'}}{\partial z} - \epsilon_v, \tag{2.7}$$

$$\frac{1}{2}\frac{\partial \overline{w'^2}}{\partial t} = \frac{g}{\theta}\overline{w'\theta'} - \frac{1}{\overline{\rho}}\overline{w'\frac{\partial p'}{\partial z}} - \frac{1}{2}\frac{\partial \overline{w'w'w'}}{\partial z} - \epsilon_w. \tag{2.8}$$

The first term of right hand side of the u and v components represents shear generation of TKE. When shear is present in the x direction, for instance when $U_g > 0$ and $V_g = 0$, the $\overline{u}$ increases with height within the boundary layer. Updraft carries air with u smaller than its surrounding, thus $\overline{u'w'}$ is negative. Since $\overline{u'w'}$ and $\frac{\partial \overline{u}}{\partial z}$ have opposite signs, the term $-\overline{u'w'}\frac{\partial \overline{u}}{\partial z}$ is positive, which means shear produces turbulence. Shear production of TKE is commonly assumed in paramterizations.

The first term of the right hand side of the w component represents buoyancy production. In convective boundary layer, potential temperature decreases with height. Updraft carries air with θ higher than its surroundings, thus $\overline{w'\theta'}$ is positive, which means turbulence is produced. The opposite is true in stable boundary layer.

The second term in each equation represents pressure transport, with p and ρ being the pressure and density of air respectively. The third term represents turbulent transport, and the last term represents dissipation.

2.3. Mean Kinetic Energy

From the budget equations of the mean horizontal velocities, one can derive the budget equations of mean kinetic energy in the x and y directions. Assuming horizontal homogeneity and ignoring horizontal and vertical advection of momentum, the budget equations of mean kinetic energy are [4]

$$\frac{1}{2}\frac{\partial}{\partial t}\overline{u}^2 = -\overline{u}\frac{\partial \overline{u'w'}}{\partial z} + f\overline{v}U_g = -\frac{\partial}{\partial z}(\overline{u}\overline{u'w'}) + \overline{u'w'}\frac{\partial \overline{u}}{\partial z} + f\overline{v}U_g \tag{2.9}$$

$$\frac{1}{2}\frac{\partial}{\partial t}\overline{v}^2 = -\overline{v}\frac{\partial \overline{v'w'}}{\partial z} - f\overline{u}V_g = -\frac{\partial}{\partial z}(\overline{v}\overline{v'w'}) + \overline{v'w'}\frac{\partial \overline{v}}{\partial z} - f\overline{u}V_g \tag{2.10}$$

U_g and V_g are the geostrophic wind components and f is the Coriolis parameter. The second term of the right hand side of this pair of equations has the same form as the first term on the right hand side of the budget equations of horizontal TKE but with opposite sign. This means that turbulence being produced results in an opposite loss of mean kinetic energy.

2.4. Parameterization of Fluxes

In weather forecast models, subgrid momentum fluxes $\overline{u'w'}$ and $\overline{v'w'}$ and heat flux $\overline{w'\theta'}$ are parameterized. There are two approaches to do so, namely the eddy diffusivity approach and the mass-flux approach.

2.4.1. Eddy Diffusivity Approach

In the eddy diffusivity approach, the heat flux $\overline{w'\theta'}$ is parameterized using the eddy diffusivity K_h, which is given as

$$\overline{w'\theta'} = -K_h\frac{\partial \overline{\theta}}{\partial z}. \tag{2.11}$$

However, countergradient heat fluxes, which refer to upward heat flux ($\overline{w'\theta'} > 0$) with $\frac{\partial \overline{\theta}}{\partial z} \leq 0$, are present in the convective boundary layer [5]. Thus, a correction term is needed [6], giving

$$\overline{w'\theta'} = -K_h\left(\frac{\partial \overline{\theta}}{\partial z} + \gamma_\theta\right). \tag{2.12}$$

Similarly, subgrid momentum fluxes $\overline{u'w'}$ and $\overline{v'w'}$ are parameterized using the eddy viscosity K_m [7]:

$$\overline{u'w'} = -K_m\frac{\partial \overline{u}}{\partial z}, \tag{2.13}$$

$$\overline{v'w'} = -K_m\frac{\partial \overline{v}}{\partial z}. \tag{2.14}$$

K_m in the x and y directions often take the same value.

2.4.2. Mass-flux Approach

In the mass-flux approach, vertical fluxes of an arbitrary field ϕ can be written as [8]

$$\overline{w'\phi'} = \kappa \sigma_u w_u (\phi_u - \phi_d). \tag{2.15}$$

Subscripts u and d denote updrafts and downdrafts respectively, while σ_u is the fractional area of updrafts. Assuming a Gaussian joint probability density function for vertical velocity and ϕ, the proportionality constant κ is approximately 0.6 [9]. Observational data of convective boundary layer topped with stratocumulus clouds show similar result [10].

The two parameterization methods described above will be compared to LES results.

3
Method

In this study, nine simulations (Case 3-11 in Table 3.1) are set up based on Salesky et al. [1]. On top of that, two stable simulations (Case 1-2) and one simulation with low shear (Case 12) are added.

For stable cases (Case 1-2), the domain size is $1.5 \times 1.5 \times 2$ km, with a $160 \times 160 \times 160$ grid. For neutral to moderately convective cases (Case 4-7), the domain size is $12 \times 12 \times 2$ km, with a $160 \times 160 \times 160$ grid. For highly convective cases (Case 8-13), the domain size is $12 \times 12 \times 3$ km, with a $160 \times 160 \times 240$ grid. The vertical grid spacing is $\Delta_z = 12.5$ m for all simulations, while the horizontal grid spacing $\Delta_x = \Delta_y$ is 9.375 m for stable cases and 75 m for other cases. A timestep of $\Delta t = 0.1$ s is used. The initial potential temperature profile is given by

$$\theta(z) = \begin{cases} 300 \text{ K}, & z \leq z_{i0} \\ 300 \text{ K} + (z - z_{i0})\Gamma_1, & z_{i0} \leq z < 1.1z_{i0} \\ 308 \text{ K} + (z - 1.1z_{i0})\Gamma_2, & z \geq 1.1z_{i0} \end{cases} \tag{3.1}$$

where $\Gamma_1 = 0.08$ K m^{-1}, $\Gamma_2 = 0.003$ K m^{-1} and z_{i0} is the initial boundary layer height. Initial turbulent kinetic energy is set to $\frac{1}{z}$ m^2 s^{-2} within the boundary layer, and 0 above the boundary layer. No moisture is included. The simulations are forced by constant geostrophic wind U_g and constant surface heat flux Q_0. U_g and Q_0 are varied systematically to obtain simulations that range from stable to neutral to convective (see Table 3.1). z_{i0} is set to 200 m for stable cases ($Q_0 < 0$) and 1000 m otherwise. The latitude is set to $\phi = 43.3°$, which corresponds to a Coriolis parameter of $f = 1.0 \times 10^{-4}$ s^{-1}. The roughness length is set to $z_0 = 0.10$ m. The simulations are run for 10 hours, which is longer than the 4-hour runs performed by Salesky et al. For the neutral simulation ($Q_0 = 0$), it is spun up with a finite heat flux of $Q_0 = 0.03$ K m s^{-1} for one hour. The namelist options of the simulations can be found in the Appendix. Table 3.1 summarizes the properties of the simulations at the end of the runs. w_* is the convective velocity scale defined as

$$w_* = \left(\frac{g}{\theta_0} Q_0 z_i\right)^{1/3}. \tag{3.2}$$

The properties of the simulations at the end of the fourth hour can be found in the Appendix.

Table 3.1: Properties of DALES runs, including geostrophic wind speed (U_g), surface heat flux (Q_0), boundary layer height (z_i), Obukhov length (L), friction velocity (u_*), and convective velocity scale (w_*) at $t = 10$ h

Case	U_g m s^{-1}	Q_0 K m s^{-1}	z_i m	$\lvert L\rvert$ m	$-z_i/L$ -	u_* m s^{-1}	w_* m s^{-1}	w_*/u_* -
1	15	-0.1	156.3	24.9	-6.27	0.33	-	-
2	15	-0.01	326.9	708.3	-0.46	0.46	-	-
3	15	0.00	1086	10^6	-0.00	0.66	0.00	0.00
4	15	0.03	1162	1139	1.02	0.78	1.04	1.34
5	15	0.07	1262	623.7	2.02	0.84	1.42	1.69
6	15	0.10	1350	470.5	2.87	0.86	1.64	1.90
7	15	0.14	1479	357.7	4.13	0.87	1.89	2.16
8	15	0.18	1672	307.8	5.43	0.90	2.14	2.37
9	15	0.24	2046	239.2	8.55	0.92	2.52	2.75
10	9	0.24	1940	83.6	23.2	0.65	2.48	3.83
11	1	0.24	1934	1.27	1520	0.12	2.48	21.2
12	0.1	0.24	1938	0.41	4776	0.06	2.48	40.6

4

Results

4.1. Overview

Figure 4.1 compares the properties of our simulations using DALES and the simulations performed by Salesky et al. [1]. Both are taken after 4 hours of simulation. The boundary layer heights in our simulations are approximately 45-80 m higher than in the simulations performed by Salesky et al., which may be due to different numerics and subgrid models used in the LES models.

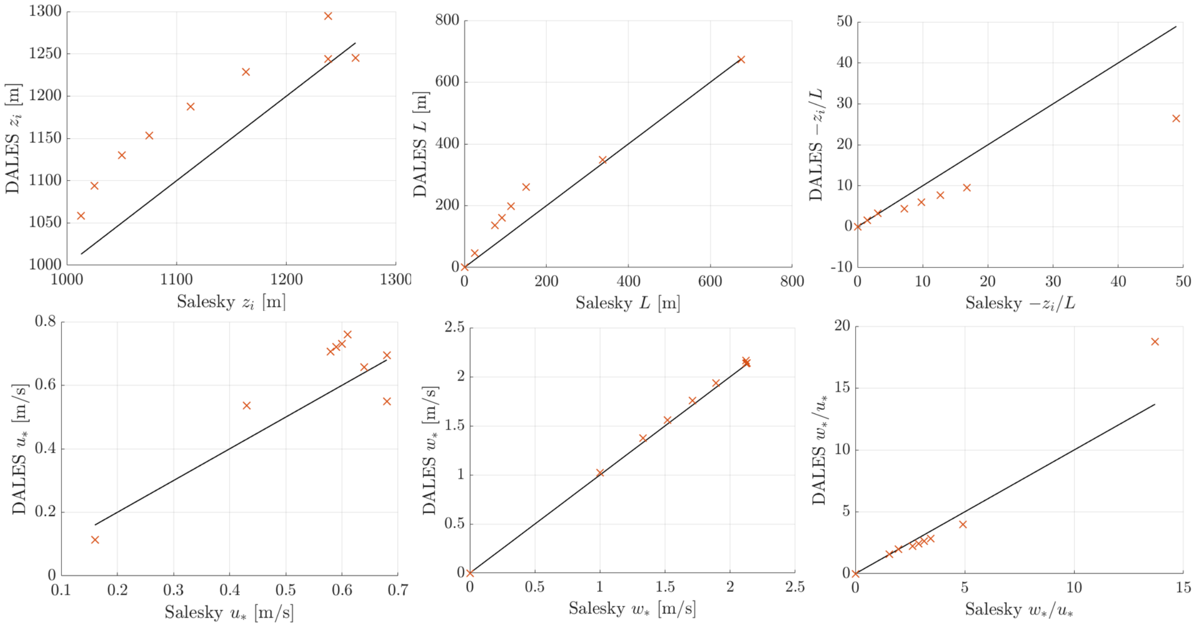

Figure 4.1: Comparison of properties of our simulations at $t = 4$ h using DALES and the simulations performed by Salesky et al. [1], with the black line showing $x = y$, and the red crosses showing the simulation results from DALES and Salesky et al. for Case 3-11 summarized in Table 3.1

Figure 4.2 shows the time evolution of the boundary layer height z_i of our simulations. The higher the value of $-z_i/L$, the more the boundary layer height grows with time. For Case 1 with large negative surface heat flux, the boundary layer height decreases with time. For all the simulations, the highest z_i is within two-third of the domain height.

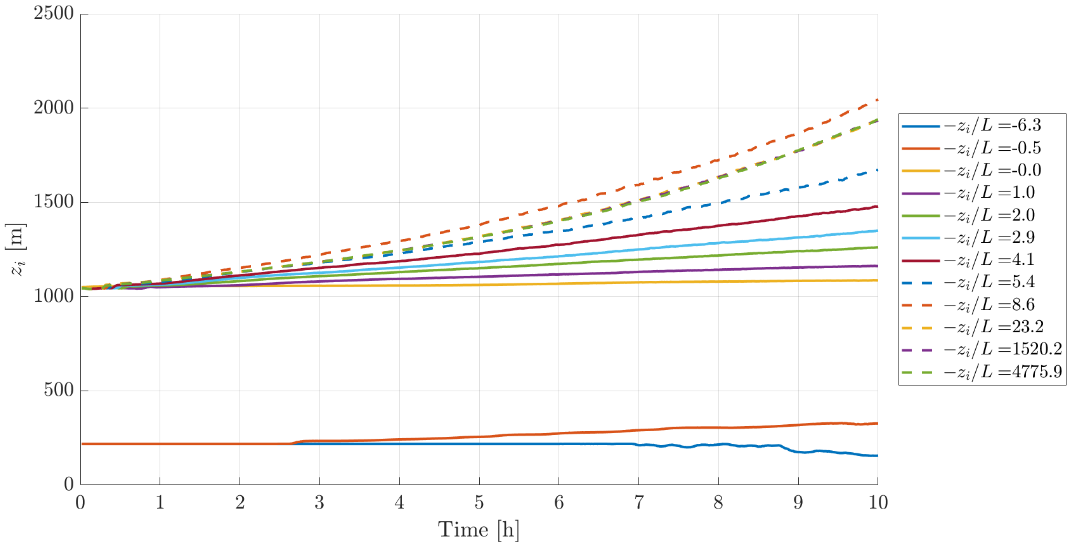

Figure 4.2: Time evolution of boundary layer height z_i for different $-z_i/L$

The left column of Figure 4.3 shows the total and resolved TKE as a function of time at $z = 50$ m for a stable simulation and a convective simulation. For both cases, the majority of the total TKE is resolved after spin up, which shows that the resolution of the simulations is sufficient. The right column of the same figure shows the total, subgrid and resolved TKE as a function of height at the end of the simulations. Near the surface, the contribution of subgrid TKE to the total TKE is larger than at the heights above, and its contribution is larger in stable cases than in convective cases.

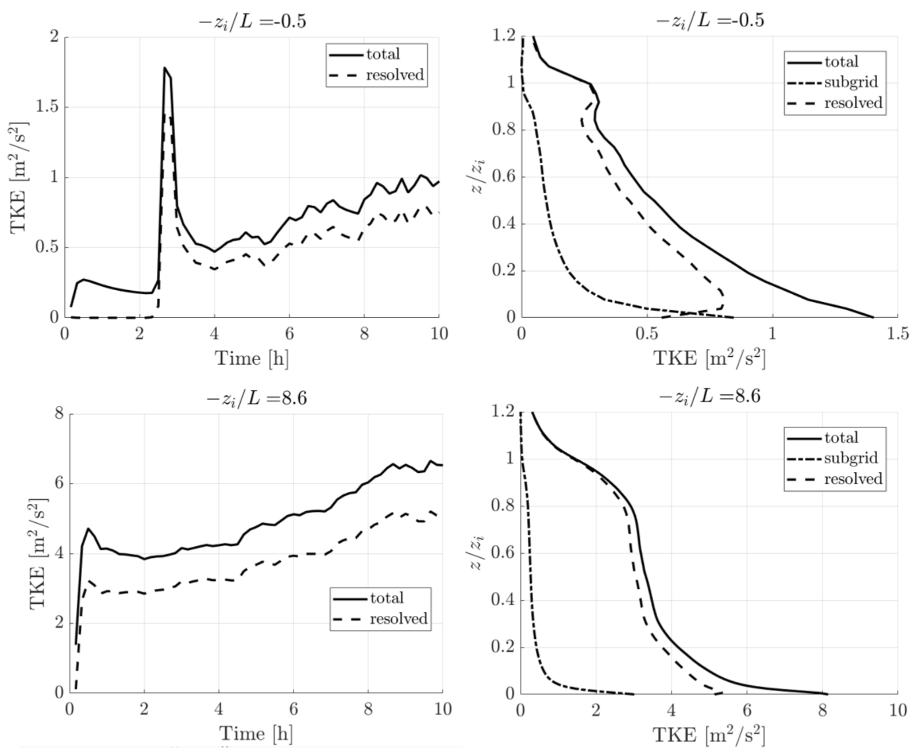

Figure 4.3: Total and resolved TKE as a function of time at $z = 50$ m (left) and as a function of z/z_i at $t = 10$ h (right) for a stable case (top row) and a convective case (bottom row)

4.2. Turbulence

In this section, we try to understand the structure of rolls in terms of turbulence.

4.2.1. Field Structure

Figure 4.4 shows the horizontal cross-section of streamwise and vertical velocities as well as potential temperature for four cases with different stability. For the stable case ($-z_i/L = -6.3$) and the weakly convective case ($-z_i/L = 2.0$), elongated patterns can be observed, which shows that rolls develop. As $-z_i/L$ increases, for $-z_i/L = 23.2$, rolls are no longer observed and cells begin to emerge. For the highly convective case ($-z_i/L = 1520.2$), cellular structures are clearly visible. Similar patterns can be observed in the horizontal cross-section of momentum and heat flux shown in Figure 4.5.

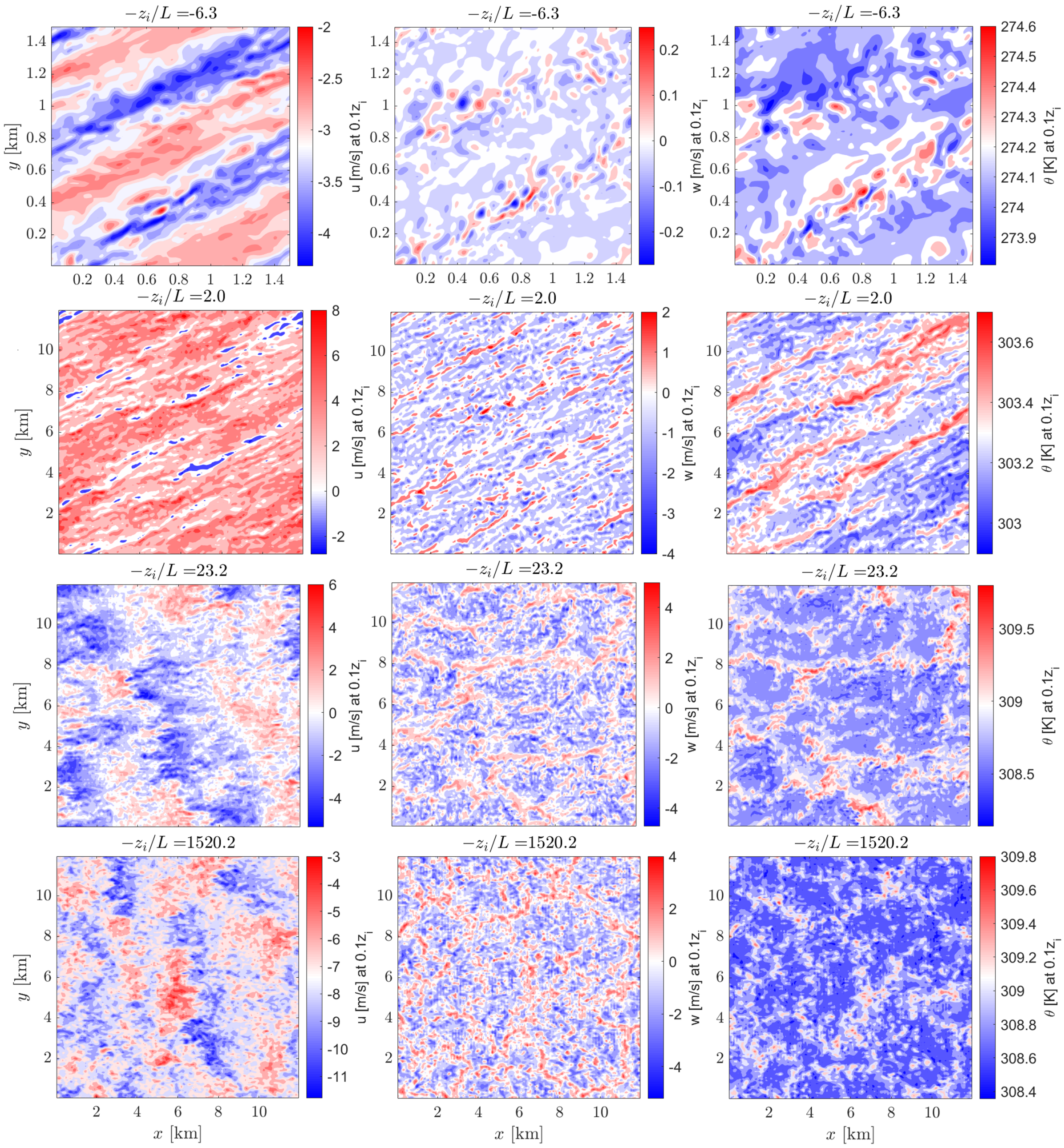

Figure 4.4: Horizontal cross-section of u (left column), w (centre column), and potential temperature θ (right column) at $z/z_i = 0.10$ at $t = 10$ h. First row $-z_i/L = -6.3$; second row $-z_i/L = 2.0$; third row $-z_i/L = 23.2$; fourth row $-z_i/L = 1520.2$

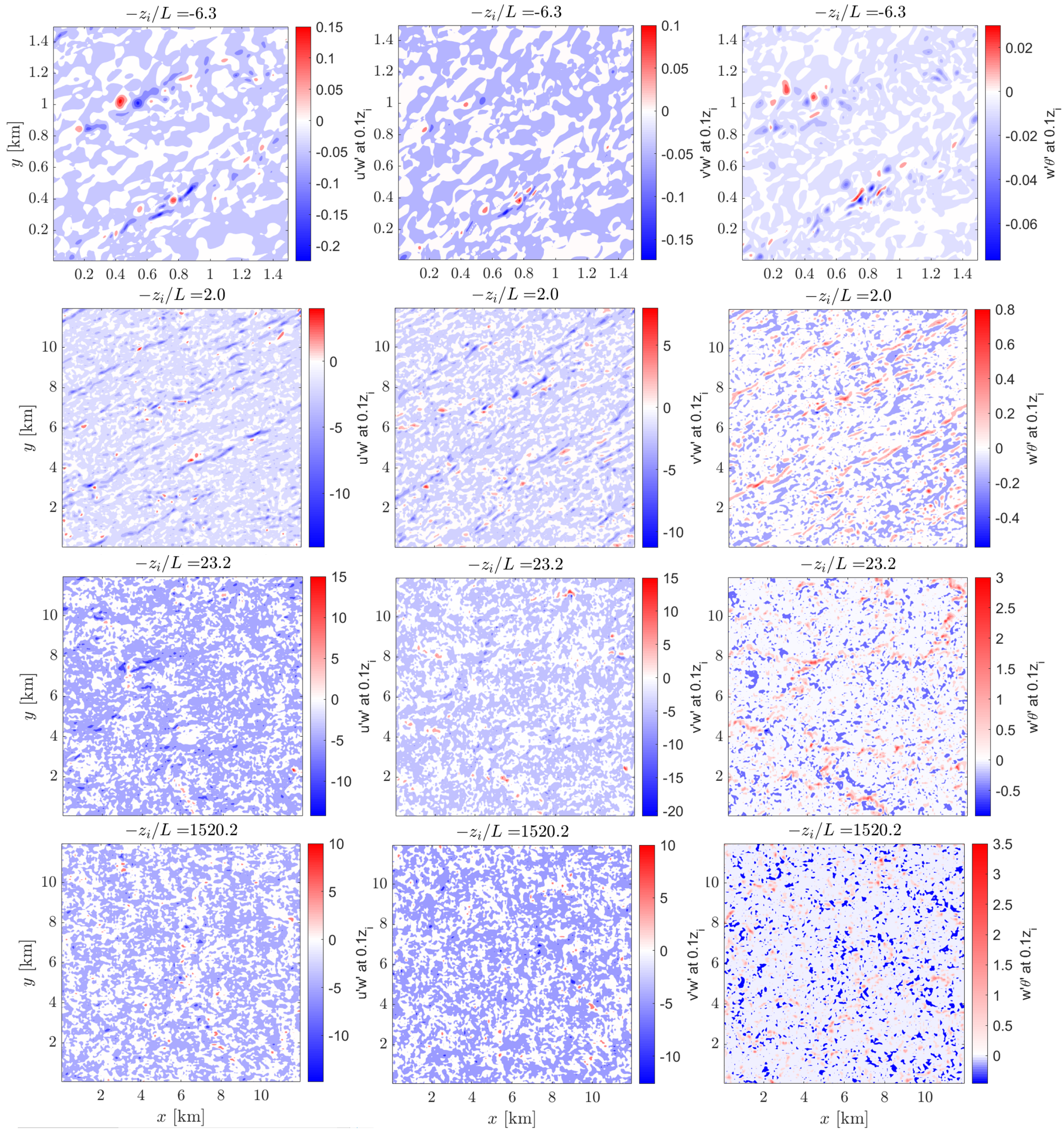

Figure 4.5: Horizontal cross-section of $u'w'$ (left column), $v'w'$ (centre column), and $w'\theta'$ (right column) at $z/z_i = 0.10$ at $t = 10$ h. First row $-z_i/L = -6.3$; second row $-z_i/L = 2.0$; third row $-z_i/L = 23.2$; fourth row $-z_i/L = 1520.2$

4.2.2. Mean Profiles

Figure 4.6 shows the vertical profiles of the slab average potential temperature and horizontal winds at the end of the simulation. In stable cases, potential temperature increases with height. In convective cases, potential temperature decreases with height near the surface. It is approximately constant within the boundary layer, forming a mixed layer, and shows an inversion at the top of the boundary layer. The potential temperature of the mixed layer increases with increasing surface heat flux.

Regarding the horizontal wind velocity, the wind speed near the surface is significantly lower due to surface friction. Above the boundary layer, the wind is geostrophic. Within the boundary layer, the wind deviates from the geostrophic wind with non-zero $\overline{v}$ due to surface friction.

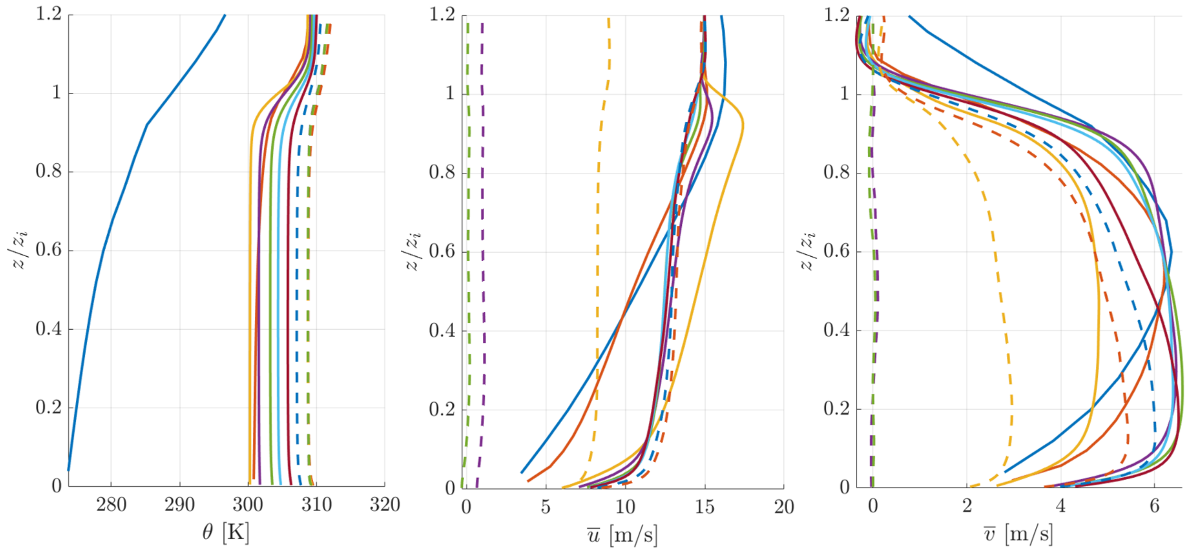

Figure 4.6: Mean potential temperature θ and horizontal wind components $\overline{u}$ and $\overline{v}$ as a function of z/z_i at $t = 10$ h of simulation. Legend is the same as that in Figure 4.2

Figure 4.7 shows the mean resolved velocity variances. $\overline{w'^2}$ increases with increasing Q_0, since more vertical turbulence is generated when buoyancy increases. $\overline{u'^2}$ and $\overline{v'^2}$ shows different profiles, which is also demonstrated in Figure 4.8. It can be seen that for situations where clear structures of rolls are observed ($-z_i/L = -$6.3-2.9), $\overline{u'^2}$ is larger than $\overline{v'^2}$, which means there is more TKE along the rolls than perpendicular to them. According to Equation 2.6 and Equation 2.7, the differences in $\overline{u'^2}$ and $\overline{v'^2}$ may come from the first term on the right hand side, which is the shear generation term. This term contains the vertical momentum flux, $\overline{u'w'}$ or $\overline{v'w'}$, which leads us to investigate these quantities next.

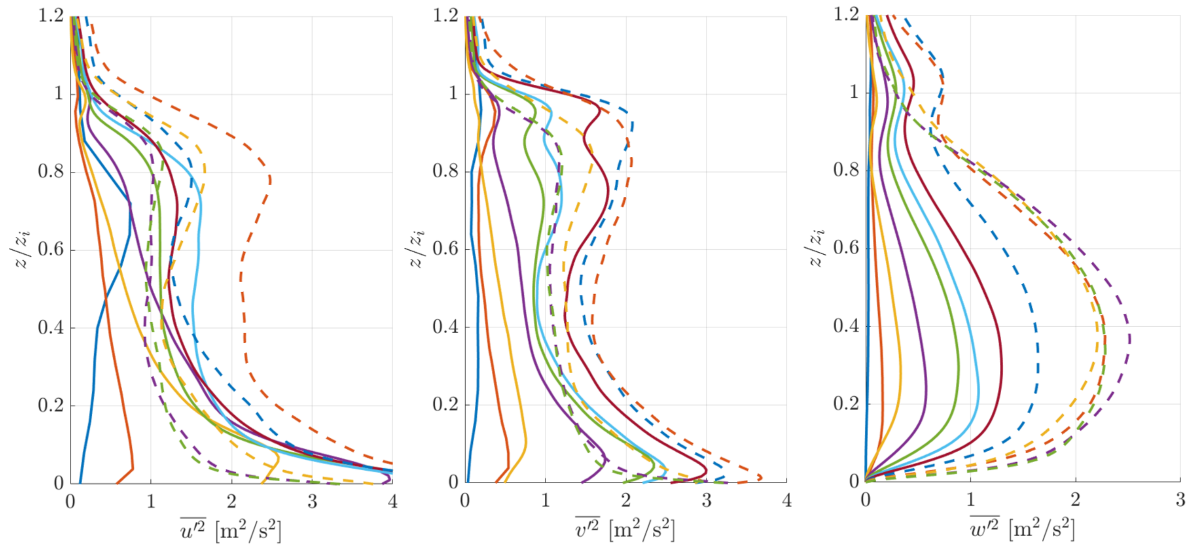

Figure 4.7: Mean resolved velocity variances as a function of z/z_i at $t = 10$ h of simulation. Legend is the same as that in Figure 4.2

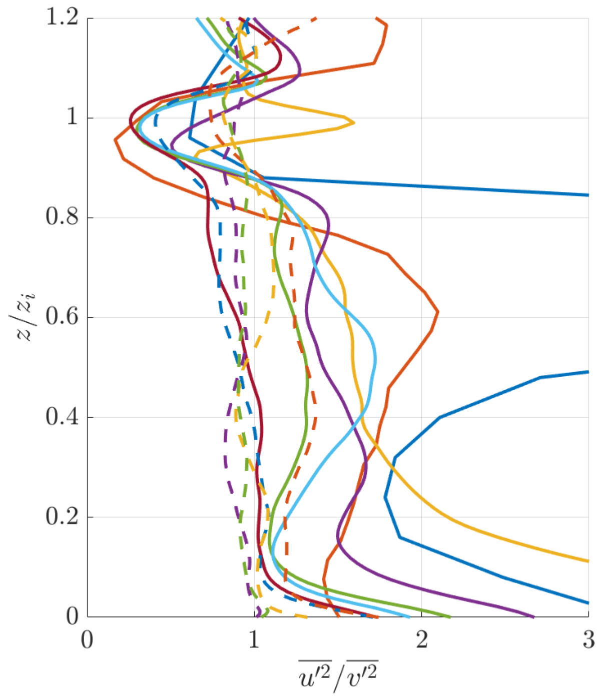

Figure 4.8: $\overline{u'^2}/\overline{v'^2}$ as a function of z/z_i at $t = 10$ h of simulation. Legend is the same as that in Figure 4.2

The left and centre figure of Figure 4.9 shows the vertical profiles of the vertical momentum fluxes. They are negative within the boundary layer for cases with a strong geostrophic wind of 9 or 15 m s^{-1}, which means that updrafts carry air with relatively small horizontal velocities. This can also be seen from Figure 4.10, which shows that horizontal velocities in updrafts are in general smaller than the overall mean. For highly convective cases with a weak geostrophic wind of 1 or 0.1 m s^{-1}, the momentum fluxes are close to zero, and the mean horizontal velocities in updrafts are approximately the same as the overall mean.

The vertical heat flux $\overline{w'\theta'}$ is shown in the right figure of Figure 4.9. For convective cases ($-z_i/L > 0$), it is positive inside the boundary layer, which means that updrafts carry air with relatively higher potential temperature. This can also be seen from the right figure in Figure 4.10, which shows that θ in updrafts are in general higher than the overall mean. Therefore, in convective boundary layer, bouyancy term in Equation 2.8 is positive, thus turbulence is produced. The contrary is true for stable cases ($-z_i/L < 0$).

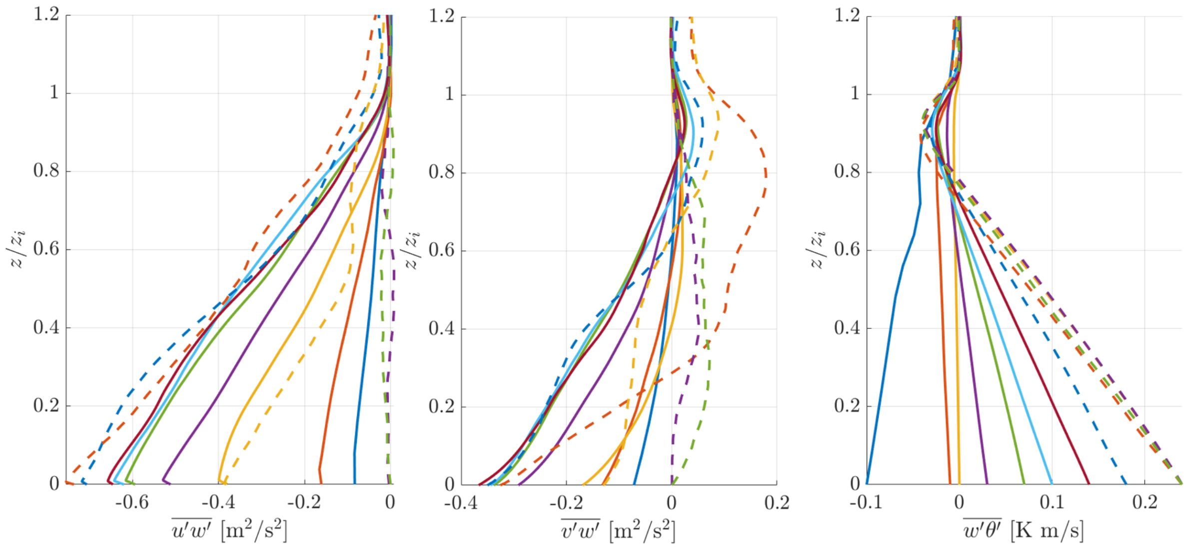

Figure 4.9: Mean total momentum fluxes ($\overline{u'w'}$ and $\overline{v'w'}$) and heat flux $\overline{w'\theta'}$ as a function of z/z_i at $t = 10$ h of simulation. Legend is the same as that in Figure 4.2

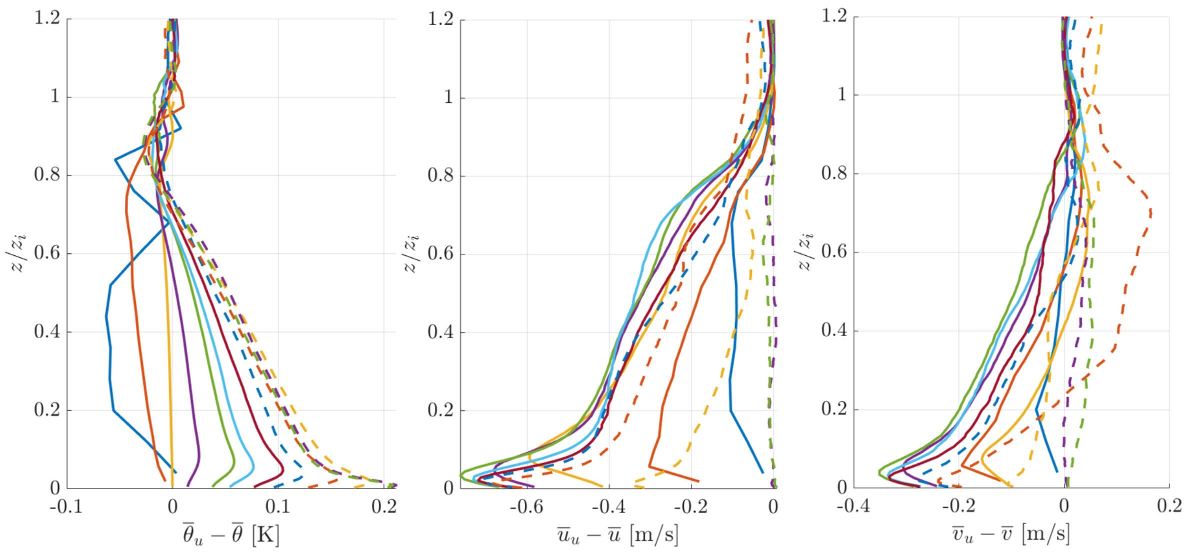

Figure 4.10: Mean values in updrafts minus overall mean for u, v and θ as a function of z/z_i at $t = 10$ h of simulation. Legend is the same as that in Figure 4.2

To explain the asymmetry of $\overline{u'^2}$ and $\overline{v'^2}$, we should consider the whole shear generation term, which involves the vertical momentum flux as well as the vertical gradient of horizontal velocity.

Figure 4.11 shows the vertical profiles of $\overline{v}$ and $\overline{v'w'}$ for the case with $-z_i/L = 2.0$. One can identify a countergradient regime (blue) bounded above by the zero-flux height where $\overline{v'w'} = 0$, and below by the zero-gradient height where $\frac{d\overline{v}}{dz} = 0$.

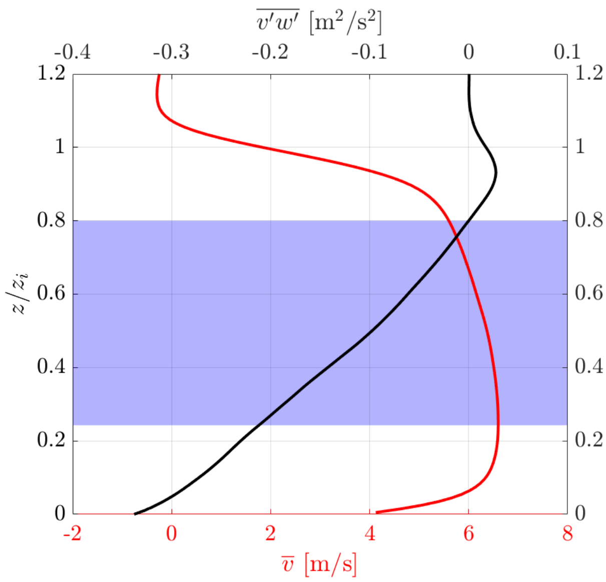

Figure 4.11: Mean profile of velocity and momentum flux in the y direction $\overline{v}$ (red) and $\overline{v'w'}$ (black), and the countergradient regime (blue shaded region) at $t = 10$ h for $-z_i/L = 2.0$

The right figure of Figure 4.12 shows the negative of the shear production term in Equation 2.7. In the countergradient regime, $-\overline{v'w'}\frac{\partial \overline{v}}{\partial z}$ is negative, which means the wind shear in the y direction destroys TKE instead of producing it, contrary to shear production in the x direction. An interpretation for this is that when rolls develop, velocity variance is generated largely along the rolls but destroyed perpendicular to the rolls.

The term $\overline{v'w'}\frac{\partial \overline{v}}{\partial z}$ also appears in the budget equation of mean kinetic energy but with an opposite sign. This means that in the countergradient regime, while TKE is destroyed, mean kinetic energy is generated. Figure 4.12 shows the three derivative terms in Equation 2.10. Although $\overline{v'w'}\frac{\partial \overline{v}}{\partial z}$ is positive and creates mean kinetic energy in the countergradient regime, the other term $-\frac{\partial}{\partial z}(\overline{v}\overline{v'w'})$ is one order of magnitude larger, which means the countergradient regime only contributes little to generating mean kinetic energy.

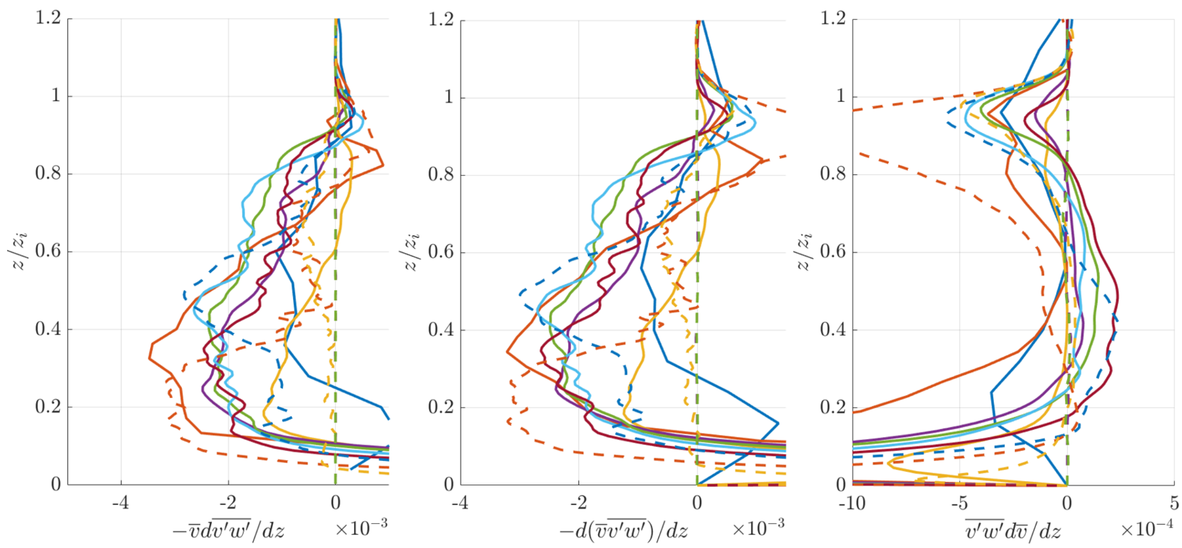

Figure 4.12: The three derivative terms in Equation 2.10 as a function of z/z_i at $t = 10$ h. Legend is the same as that in Figure 4.2

4.3. Parameterization

In this section, we will discuss how the asymmetry in the x and y directions when rolls develop may influence the paramterization of fluxes in weather and climate models.

4.3.1. Eddy Diffusivity Approach

Figure 4.13 shows the vertical profile of eddy diffusivity K_h diagnosed from the vertical heat flux and mean potential temperature profiles. A countergradient regime is present in all convective cases with $-z_i/L > 0$.

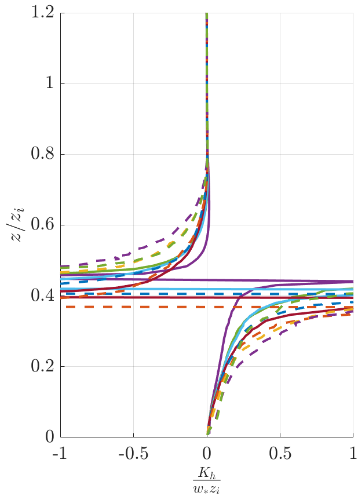

Figure 4.13: Normalised eddy diffusivity K_h as a function of z/z_i at $t = 10$ h. Legend is the same as that in Figure 4.2

The left and centre figures of Figure 4.14 show the eddy viscosity profiles for u and v diagnosed from the momentum flux and mean horizontal velocity profiles. $K_{m,v}$ becomes negative within the boundary layer as a consequence of a countergradient regime. A countergradient correction term could be introduced in Equation 2.14 to improve the parameterization of $\overline{v'w'}$, similar as Equation 2.12 proposed by Holtslag and Moeng [6].

The right figure of Figure 4.14 shows the ratio of K_m for v and u. The ratio is not equal to one for most cases, which means they are not equal. It might be necessary to prescribe different values for them in numerical weather prediction models and climate models in situations where rolls develop.

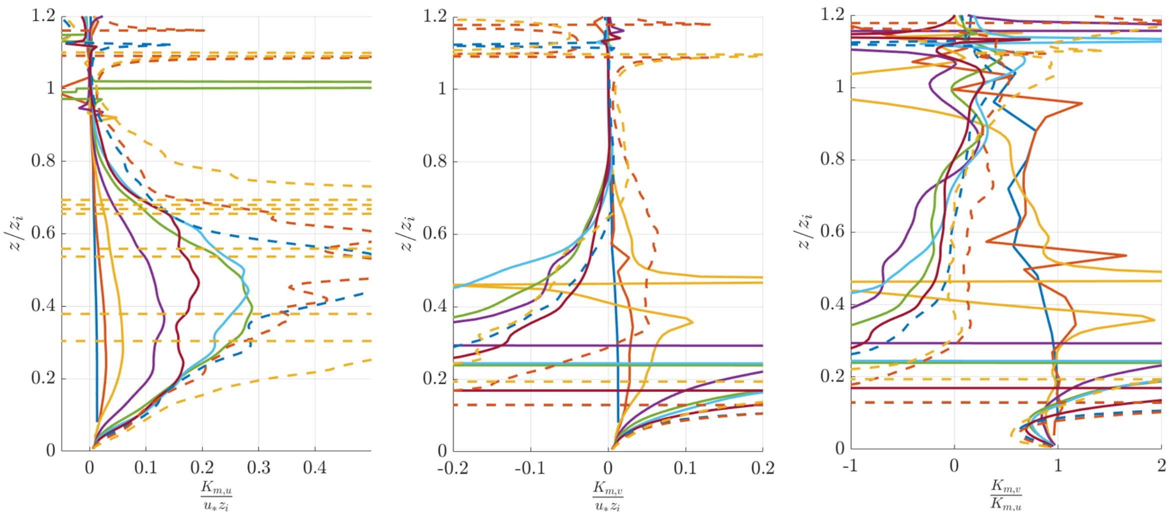

Figure 4.14: Normalised eddy viscosity $K_{m,u}$ and $K_{m,v}$ and their ratio as a function of z/z_i at $t = 10$ h. Legend is the same as that in Figure 4.2

At this point, we will address the non-stationarity of the countergradient regime for $\overline{v'w'}$. Figure 4.15 shows how the countergradient regime depends on $-z_i/L$ at different times of the simulations. In weakly convective boundary layer ($-z_i/L =$ 1.0-5.4), the position and depth of the countergradient regime is approximately constant with time. An example is shown in the centre figure of Figure 4.16. For more convective cases ($-z_i/L =$ 8.6-22.3), the zero-gradient height increases with time and the zero-flux height decreases with time, causing the countergradient regime to become shallower with time. An example is shown in the right figure of Figure 4.16. It is also evident from the right figure of Figure 4.16 that the extent of the countergradient regime varies with time, which means it is non-stationary. For highly convective boundary layer where cells develop, since the momentum fluxes are close to zero throughout the boundary layer, the zero-flux height is not well-defined, thus there is no well-defined countergradient regime. Interestingly, in stable or neutral boundary layer where rolls develop, the zero-flux and zero-gradient heights collapse, thus the countergradient regime does not exist. An example is shown in the left figure of Figure 4.16.

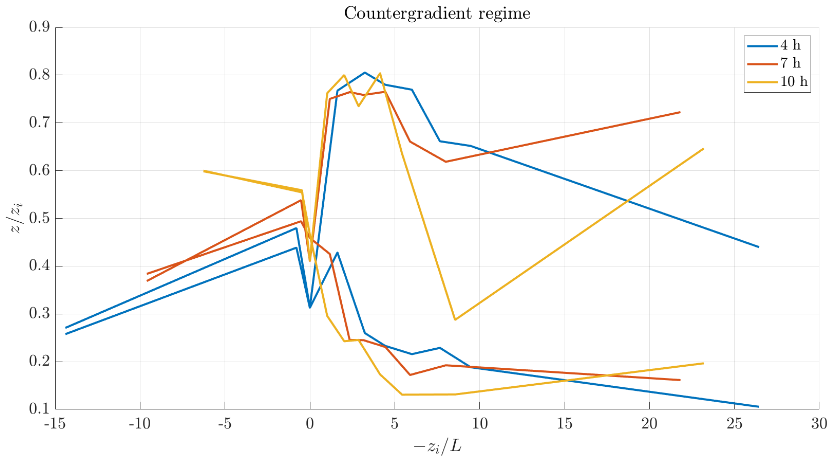

Figure 4.15: Boundaries of countergradient regime for $\overline{v'w'}$ as a function of $-z_i/L$ at $t =$4, 7 and 10 h

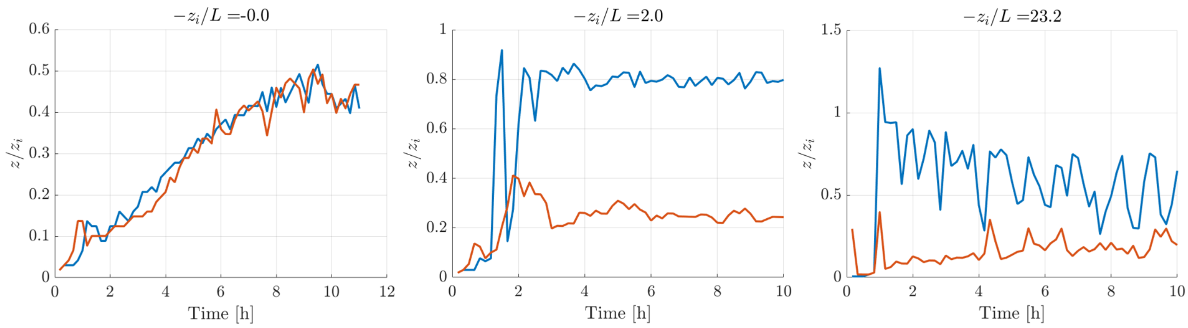

Figure 4.16: Time evolution of the countergradient regime for $\overline{v'w'}$. Blue: zero-flux height, red: zero-gradient height

4.3.2. Mass-flux Approach

Figure 4.17 shows the plot of $\sigma_u w_u(\phi_u - \phi_d)$ against $\overline{w'\phi'}$ for $\phi = \theta$, u and v. It can be seen that in the boundary layer, the proportionality constant κ in Equation 2.15 is approximately equal to 0.6, which is consistent to results in the literature [9, 10]. In the surface layer ($z < 100$ m) where $\overline{w'\theta'}$ is large and $\overline{u'w'}$ and $\overline{v'w'}$ is highly negative, κ deviates from the value of 0.6.

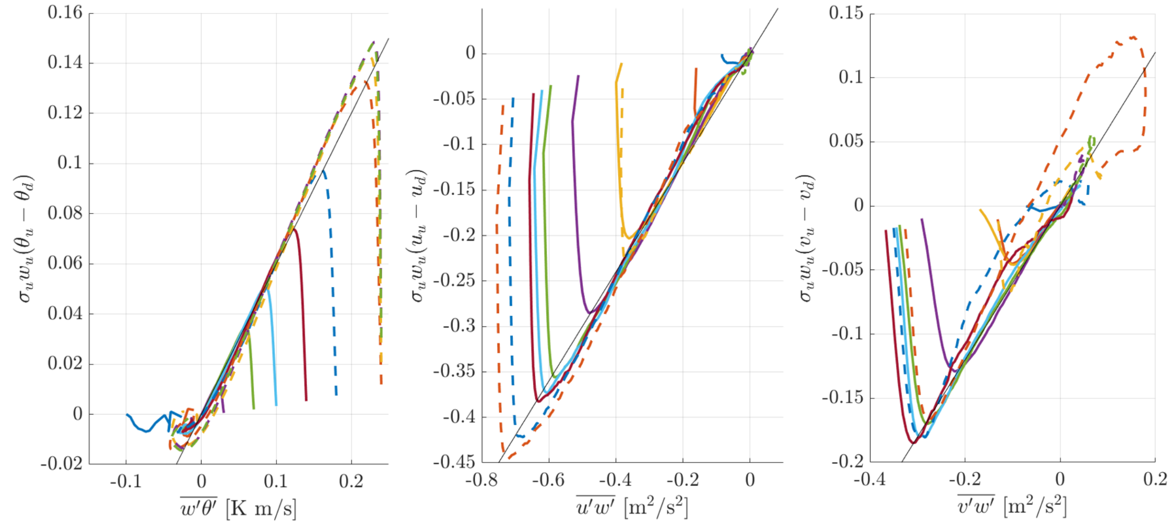

Figure 4.17: Vertical fluxes of the mass-flux model ($\sigma_u w_u(\phi_u - \phi_d)$) as a function of the simulated vertical fluxes ($\overline{w'\phi'}$) for $\phi = \theta$, u and v. The thin black line has a slope of 0.6. Legend is the same as that in Figure 4.2

5

Conclusion

In this study, the simulations performed by Salesky et al. are produced using DALES and roll structures are observed in stable to moderately convective boundary layer ($Q_0 = -6.3$ - 8.6 K m s^{-1} when an east-west geostrophic wind is present. The asymmetry of rolls in the x and y directions is studied in terms of turbulence. It is shown that the turbulent kinetic energy in the x and y directions are not equal when rolls are formed. By investigating the shear generation term in the TKE budget equations of the x and y directions, it is found that a countergradient regime is present for $\overline{v'w'}$. In the countergradient regime, TKE in the y direction is destroyed by shear, contrary to being produced in the x direction. While TKE in the y direction is destroyed, mean kinetic energy in the same direction is generated.

The asymmetry in the x and y directions when rolls develop also suggests that the eddy viscosity K_m for the x and y directions would be rather different. The presence of a countergradient regime for $\overline{v'w'}$ but not for $\overline{u'w'}$ means that a countergradient correction term may need to be included when parameterizing $\overline{v'w'}$. However, the countergradient regime is non-stationary when $-z_i/L$ increases, while it does not exist in neutral or stable boundary layers with rolls. Hence, the design of an improved parameterization scheme is non-trivial.

Appendix

Namoptions

```
&RUN
iexpnr     =  001
runtime    =  36000
dtmax      =  0.1
ladaptive  =  .false.
lwarmstart =  .false.
irandom    =  43
randthl    =  0.1
randqt     =  1e−5
nprocx     =  4
/
&DOMAIN
itot       =  160
jtot       =  160
kmax       =  160
xsize      =  1500.
ysize      =  1500.
xlat       =  43.3
xlon       =  0
xtime      =  4.
/
&PHYSICS
ps         =  102000.00
thls       =  300.
lcoriol    =  .true.
iradiation =  0
z0         =  0.1
/
&NAMSURFACE
wtsurf     = −0.1
wqsurf     = 0
isurf      = 4
/
&DYNAMICS
cu         =  8.
cv         =  0.
iadv_mom   =  2
iadv_tke   =  2
iadv_thl   =  2
iadv_qt    =  2
/
&NAMSUBGRID
ldelta          = .true.
sgs_surface_fix = .true.
/
&NAMCHECKSIM
tcheck     = 5
/
&NAMTIMESTAT
ltimestat  = .true.
dtav       = 60
/
```

```
&NAMGENSTAT
lstat       = .true.
dtav        = 60
timeav      = 600
/
&NAMBUDGET
lbudget     = .true.
dtav        = 60
timeav      = 600
/
&NAMNETCDFSTATS
lnetcdf     = .true.
/
&NAMSAMPLING
dtav        = 60
timeav      = 600
lsampup     = .true.
lsampbuup   = .true.
/
&NAMFIELDDUMP
dtav        = 3600.0
lfielddump  = .true.
/
```

Properties of DALES runs at $t = 4$ h

Table 1: Properties of DALES runs, including geostrophic wind speed (U_g), surface heat flux (Q_0), boundary layer height (z_i), Obukhov length (L), friction velocity (u_*), and convective velocity scale (w_*) at $t = 4$ h

Case	U_g m s^{-1}	Q_0 K m s^{-1}	z_i m	$\|L\|$ m	$-z_i/L$ -	u_* m s^{-1}	w_* m s^{-1}	w_*/u_* -
1	15	-0.1	218.3	15.2	-14.4	0.28	-	-
2	15	-0.01	242.2	305.7	-0.79	0.34	-	-
3	15	0.00	1059	10^6	-0.00	0.55	0.00	0.00
4	15	0.03	1094	673.6	1.62	0.66	1.02	1.56
5	15	0.07	1130	349.2	3.24	0.69	1.37	1.98
6	15	0.10	1154	259.9	4.44	0.71	1.56	2.21
7	15	0.14	1188	197.7	6.01	0.72	1.76	2.44
8	15	0.18	1229	160.4	7.66	0.73	1.93	2.65
9	15	0.24	1295	136.7	9.47	0.76	2.17	2.85
10	9	0.24	1244	47.0	26.5	0.54	2.14	3.99
11	1	0.24	1245	1.06	1179	0.11	2.14	18.8
12	0.1	0.24	1246	0.39	3173	0.06	2.14	33.1

Bibliography

[1] S. T. Salesky, M. Chamecki, and E. Bou-Zeid, “On the nature of the transition between roll and cellular organization in the convective boundary layer,” *Boundary-layer meteorology*, vol. 163, no. 1, pp. 41–68, 2017.

[2] T. Heus, C. C. van Heerwaarden, H. J. J. Jonker, A. P. Siebesma, S. Axelsen, K. Van Den Dries, O. Geoffroy, A. F. Moene, D. Pino, S. R. De Roode, *et al.*, “Formulation of the dutch atmospheric large-eddy simulation (DALES) and overview of its applications,” *Geoscientific Model Development*, vol. 3, no. 2, pp. 415–444, 2010.

[3] R. B. Stull, *An introduction to boundary layer meteorology*, vol. 13. Springer Science & Business Media, 1988.

[4] B. Saggiorato, L. Nuijens, A. P. Siebesma, S. R. de Roode, I. Sandu, and L. Papritz, “The influence of convective momentum transport and vertical wind shear on the evolution of a cold air outbreak,” *Journal of Advances in Modeling Earth Systems*, vol. 12, no. 6, p. e2019MS001991, 2020.

[5] J. W. Deardorff, “The counter-gradient heat flux in the lower atmosphere and in the laboratory,” *Journal of Atmospheric Sciences*, vol. 23, no. 5, pp. 503 – 506, 1966.

[6] A. A. M. Holtslag and C.-H. Moeng, “Eddy diffusivity and countergradient transport in the convective atmospheric boundary layer,” *Journal of Atmospheric Sciences*, vol. 48, no. 14, pp. 1690 – 1698, 1991.

[7] P. Baas, S. R. de Roode, and G. Lenderink, “The scaling behaviour of a turbulent kinetic energy closure model for stably stratified conditions,” *Boundary-layer meteorology*, vol. 127, pp. 17–36, 2008.

[8] A. P. Siebesma, “On the mass flux approach for atmospheric convection,” in *Proc. Workshop on New Insights and Approaches to Convective Parametrization*, pp. 25–57, 1996.

[9] J. C. Wyngaard and C.-H. Moeng, “Parameterizing turbulent diffusion through the joint probability density,” *Boundary-layer meteorology*, vol. 60, pp. 1–13, 1992.

[10] A. T. J. De Laat and P. G. Duynkerke, “Analysis of ASTEX-stratocumulus observational data using a mass-flux approach,” *Boundary-layer meteorology*, vol. 86, pp. 63–87, 1998.